CMS Physics Analysis Summary

Search for $H^+ \to c\bar{b}$ in lepton+jets channel using top quark pair events

The CMS Collaboration

Abstract

Results on the search for a light charged Higgs boson H^+ decaying to $c\bar{b}$ in top quark pair events using the CMS detector at the LHC are presented. The total dataset corresponds to 19.7 fb^{-1} of proton-proton collisions at $\sqrt{s}$ = 8 TeV. In $t\bar{t}$ decays, if one top quark decays to H^+b, instead of Wb, and the H^+ subsequently decays to $c\bar{b}$, while other top quark decays leptonically ($\bar{t} \to W^-\bar{b} \to l\bar{\nu}\bar{b}$)), the final state then consists of four jets (three b quark jets), one lepton (electron or muon), and missing energy: $t\bar{t} \to (H^+b)(W^-\bar{b}) \to (c\bar{b}b)(l\bar{\nu}\bar{b})$. The main observable used in the analysis is an invariant mass of two jets, one of which is identified as a b quark jet. The dijet pair is selected from at least four jets in an event by a dedicated kinematic fitter. No signal for the presence of a charged Higgs boson is observed and upper limits are set at 95% confidence level on the branching ratio for t $\to H^+b$ from 1.1–0.4% for the charged Higgs boson mass in the range 90–150 GeV in the assumption of branching ratio of $B(H^+ \to c\bar{b})$ = 100% for the first time.

1 Introduction

The Higgs boson was discovered at a mass of 125 GeV in 2012 [1, 2] and its properties [3–6] so far have been found to agree with those of the Higgs boson, an integral part of the standard model (SM) [7–9]. This discovery shed a light on the mystery of spontaneous symmetry breaking which had been pursued for 50 years since it was proposed [10–15]. Although the final missing parameter of the SM was found, many questions still remain unexplained in the scope of the SM. Thereby several hypotheses beyond the SM (BSM) have been tested to solve these questions.

In many BSM scenarios, there are more than one Higgs boson, some of which can be charged. For example, two Higgs doublet models (2HDM) [16, 17] predict five Higgs bosons: two charged ($H^{\pm}$) and three neutral Higgs bosons (A^0, H^0, h^0), and the observed 120 GeV boson would be just one of the CP-even neutral bosons (H^0 or h^0). Unlike in the SM, in the 2HDM flavour changing neutral current (FCNC) occurs at tree level because Yukawa couplings are not flavour diagonal. In order to supress the tree level FCNC, all fermions which have the same quantum numbers are supposed to couple to the same Higgs multiplet [18, 19]. The 2HDM is categorized into four different types of models depending on the assignment of how the right-handed charged quarks and leptons couples to Higgs fields; type-I, type-II, type-X, and type-Y. Table 1 summarizes each model that leads to natural flavour conservation.

Table 1: Four 2HDM models with each right-handed fermions coupling to each of two Higgs doublets. Each model leads to natural flavour conservation.

Model	Up-type Quarks	Down-type Quarks	Charged Leptons
Type-I	Φ_2	Φ_2	Φ_2
Type-II	Φ_2	Φ_1	Φ_1
Lepton-specific(Type-X)	Φ_2	Φ_2	Φ_1
Flipped(Type-Y)	Φ_2	Φ_1	Φ_2

Here we search for a charged Higgs boson that is predicted in the 2HDM model. In this model the mass of the charged Higgs boson (H^+) is an unknown parameter, but it is expected to have a large coupling to the top quark. If the mass of the charged Higgs boson is less than the top quark mass (so-called a light charged Higgs boson scenario), the top quark can decay to the charged Higgs boson, t→H^+b. The light charged Higgs boson has been directly searched in $H^+ \rightarrow \bar{\tau}\nu$ [20–24] and $H^+ \rightarrow c\bar{s}$ [25–28] decays at hadron collider experiments. The charged Higgs boson has not been observed in top quark decays in these two channels and upper limits on the branching ratio of t→H^+b is placed at O(1%).

In the search presented here the light charged Higgs boson decay channel $H^+ \rightarrow c\bar{b}$ is considered (the charge conjugated state is implied). This decay branching ratio is enhanced and dominant in the type-Y 2HDM model [29, 30].

If the t→H^+b $\rightarrow c\bar{b}$b process takes place, the best channel to find such decays is t$\bar{t}$ production, with one top quark decaying to the charged Higgs boson and subsequently giving three jets, two of which originate from b-quarks, while the other top quark via the SM leptonic decay $\bar{t} \rightarrow W^-\bar{b} \rightarrow \ell\bar{\nu}$b. This gives a final state with three b-jets, compared with two from the semi-leptonic SM t$\bar{t}$ decay. In the SM t$\bar{t}$ decay the invariant mass of the two un-tagged jets will peak at the W mass. However, in this case of t→H^+b $\rightarrow c\bar{b}$b decays, the dijet invariant mass will peak at the mass of the charged Higgs boson. Figure 1 shows the dijet mass distribution for two jets from H^+ and W decays in t$\bar{t}$ events. This analysis searches for a charged Higgs boson by looking for a second peak in this dijet mass spectrum in t$\bar{t}$ decays. The analysis takes advantage

of the additional b quark in the final state, and divides the search into events with 2 b-tagged jets and events with at least 3 b-tagged jets.
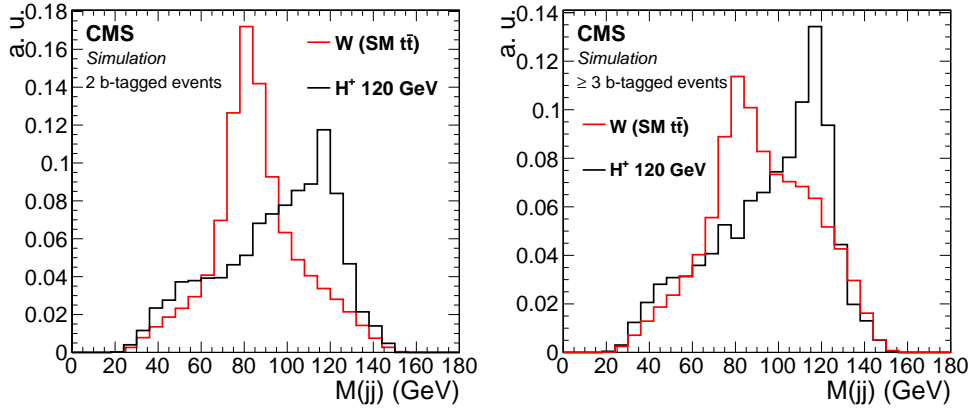

Figure 1: Expected dijet mass distribution for W from SM $t\bar{t}$ and from H^+ signal $t\bar{t}$ in the events with two b-tagged jets (left), and with more than two b-tagged events (right).

This search is performed using CMS data collected at $\sqrt{s}$ = 8 TeV, with a total integrated luminosity of 19.7 fb^{-1}. The datasets and simulation samples used in the analysis are described in Section 2 and 3. The event selection criteria are listed in Section 4. Section 5 describes the background estimation used in this search. Energy corrections for the jets in the selected events are explained in Section 6 while the kinematic fitter used for sorting jets in the event is presented in Section 7. Section 8 summarizes systematic uncertainties. Fit on the observed data and the upper limits on B(t→H$^+$b) with 95% C.L. are presented in Section. 9. The summary of the search is given in Section 10.

2 CMS detector and Event reconstruction

The central feature of the CMS detector is a superconducting solenoid with an internal radius of 3 m. The solenoid provides a magnetic field of 3.8 T along the direction of the beam, which represent the z-axis of the detector coordinate system, with the center of the detector defined to be at z = 0. The azimuthal angle ϕ is measured in the plane perpendicular to the z axis, while the polar angle θ is measured with respect to this axis. Within the superconducting solenoid volume are a silicon pixel and strip tracker, a lead tungstate crystal electromagnetic calorimeter (ECAL), and a brass and scintillator hadron calorimeter (HCAL), each composed of a barrel and two endcap sections. The electromagnetic calorimeter provides a coverage in pseudorapidity $|\eta| < 1.479$ in the barrel region (EB) and $1.479 < |\eta| < 3.0$ in the two endcap regions (EE), where we define pseudorapidity as $\eta = -\ln[\tan(\theta/2)]$. Muons are measured in gas ionization detectors embedded in the steel return yoke. Extensive forward calorimetry complements the coverage provided by the barrel and endcap detectors.

The first level of the CMS trigger system, composed of custom hardware processors, uses information from the calorimeters and muon detectors to select up to 100 kHz of the most interesting events. The High Level Trigger (HLT) processor farm uses information from all CMS subdetectors to further decrease the event rate to roughly 300 Hz before data storage. The LHC provided luminosity is measured using the forward calorimeters and pixel detector. A more detailed description of the CMS detector, as well as definitions of the coordinate system used, can be found in Ref. [31].

Final state objects used in this analysis are reconstructed using the standard CMS particle-flow (PF) algorithm [32]. This algorithm reconstructs five different types of objects–muons, electrons, photons, neutral hadrons, and charged hadrons–coherently exploiting all the CMS sub-detectors. It also reconstructs vertices using associated tracks.

Electron candidates are reconstructed in pseudorapidity range $|\eta| < 2.5$ by associating electro-magnetic depositions in the ECAL with reconstructed charged tracks in the tracking system. Muons are identified in pseudorapidity range $|\eta| < 2.4$ by matching tracks reconstructed in the muon system and the central tracker.

Jets are clustered using all the particle flow candidates except isolated leptons and charged hadrons from non-primary vertices. The anti-kt algorithm [33] with a distance parameter (ΔR) of 0.5 is used. A series of corrections [34] are applied to the jet energy-momentum 4-vector in order to account for the effect of pileup, non-uniform detector response, and residual data-simulation differences. The missing transverse momentum vector is defined as the projection on the plane perpendicular to the beams of the negative vector sum of the momenta of all reconstructed particles in an event. Its magnitude is referred to as E_T^{miss}.

3 Simulation samples

The charged Higgs boson signal events are simulated using the generator PYTHIA [35]. In this process $t\bar{t}$ events are produced, where the top quark decays to H^+ and a b quark and anti-top quark to W^- and $\bar{b}$. The charged Higgs boson is then decayed to $c\bar{b}$, and the W decays to an electron or a muon and an accompanying neutrino.The charge conjugate state ($H^- \rightarrow \bar{c}b$) is also simulated. We assume a very small ($\sim$ zero) width of the charged Higgs boson. The signal $t\bar{t}$ samples are prepared for the H^+ masses of 90, 100, 110, 120, 130, 140, and 150 GeV.

Background samples, including SM $t\bar{t}$ which is the dominant background, are mainly generated with MADGRAPH 5.1.3.30 [36]. The exceptions are single top quark and diboson samples for which POWHEG v1.0 r1380 [37] and PYTHIA are used respectively.

Parton showering and hadronization are simulated using PYTHIA v6.4 [35]. These samples include the full simulation of the CMS detector based on GEANT4 [38] and simulated events are reconstructed using the same CMS software as used for data. To ensure correct simulation of the number of additional interactions per bunch crossing (pileup), simulated events are mixed with multiple minimum bias events. Each simulated event is then weighted such that the distribution of pileup interactions in the simulation matches that of the real data.

4 Event Selection

Signal events, $t\bar{t}\rightarrow b(H^+)\bar{b}W^-\rightarrow b\bar{b}(c\bar{b})\ell\nu$, contain one prompt lepton, one neutrino, and four quarks, three of which are b quarks. Therefore we expect the final state to consist of either a muon or an electron, at least four jets and missing transverse energy. This section describes the selection of the final state objects and events to be used in the analysis.

In both the muon and electron channels events are selected using single lepton triggers. For the muon channel the trigger requires an isolated single muon with a p_T threshold of 24 GeV and upper $|\eta|$ threshold of 2.1. While for the electron channel the trigger selects events by requiring a single isolated electron with a p_T greater than 27 GeV and $|\eta|$ smaller than 2.5. Events are first required to contain a well reconstructed primary vertex, where the primary vertex is assigned to the vertex with the highest $\sum p_{T\,tracks}^2$ in the event.

For the H$^+$ search events are selected by requiring exactly one lepton, at least four jets and large missing transverse energy. This analysis uses both the electron and muon channels. The electron (muon) candidates are required to have a p_T larger than 30 (26) GeV, $|\eta| < 2.5$ (2.1) and must be consistent with originating from the primary vertex. Electron candidates must pass a number of identification requirements on the shower shape, track quality and matching between the track and supercluster. Electrons directing to the barrel-endcap transition gap (1.4442 $< |\eta_{sc}| < 1.5660$) are excluded. Electrons that are consistent with being due to a photon conversion are vetoed. The electrons must be well isolated from other activity in the event, which is ensured by requiring their relative isolation parameter (Iso$_{rel}$) to be less than 0.1. Here Iso$_{rel}$ is defined as the scalar sum of momenta of PF objects within $\Delta R = \sqrt{(\Delta \eta)^2 + (\Delta \phi)^2} < 0.3$ of the candidates direction, excluding the candidate itself, divided by the lepton candidates transverse momentum. A set of track quality cuts are applied to the muon selection [39]. Similar to electron candidates, muon candidates are required to be isolated with Iso$_{rel} < 0.12$. For muons Iso$_{rel}$ is calculated in a cone $\Delta R < 0.4$. No other e(or μ) with a looser requirement of $p_T > 20$ (10) GeV within $|\eta| < 2.5$ and relative isolation less than 0.3 are allowed.

Jets are selected that have $p_T > 30$ GeV and must be within the tracker coverage of $|\eta| < 2.4$, while additional quality cuts are applied to remove fake jets reconstructed from detector noise. Since this analysis looks for events which include a neutrino in the final state, we require $E_T^{miss} > 20$ GeV.

The signal events, $t\bar{t} \rightarrow (H^+b)(Wb) \rightarrow (cbb)(\ell \nu b)$, have three b quarks in the final state, while the SM decays, $t\bar{t} \rightarrow (Wb)(Wb) \rightarrow (jjb)(\ell \nu b)$, give only two b quarks. We use the combined secondary vertex tagger to identify jets originating from b quarks , with the medium working point, defined such that the misidentification rate is 1% while the b-tagging efficiency is $\sim$ 70% [40]. Events with two or more b-tagged jets are taken as a signal region, while events with only one b-tagged jet are used as a control sample as discussed in Section 5.

The analysis uses four event categories (signal regions) in total, depending on the lepton flavour and number of b-tagged jets, which are defined as:

1. Electron + E_T^{miss} + four or more jets, with two of the four leading jets b-tagged (electron 2b-tag signal region);

2. Electron + E_T^{miss} + four or more jets, with three of the four leading jets b-tagged (electron 3b-tag signal region);

3. Muon + E_T^{miss} + four or more jets, with two of the four leading jets b-tagged (muon 2b-tag signal region);

4. Muon + E_T^{miss} + four or more jets, with three of the four leading jets b-tagged (muon 3b-tag signal region);

5   Background Estimation

In this analysis we consider three types of backgrounds. These include backgrounds from top quark, such as $t\bar{t}$ and single top quark decays, backgrounds which are not associated with top quark (non-top backgrounds), and QCD multijet events where a jet is misidentified as a non-prompt lepton. It is important to note here that the SM $t\bar{t}$ background is scaled down with the appearance of signal, t$\rightarrow$H$^+$b, to account for the change in branching ratio of the SM decays.

In the 2 b-tag region the estimation of the top quark and non-top backgrounds are both done using simulation. A number of corrections are applied to the simulated events to better model

the data. Non-top backgrounds here include for example events from boson+jets (where boson is either W or Z) or diboson+jet.

The 3 b-tags events from SM $t\bar{t}$ decays have two components: $t\bar{t}$+jets (where jets come from gluons and light quarks and one of these jets is mis-tagged) and $t\bar{t} + b\bar{b}$. Simulation of the latter process is known to give too few events [41, 42]. To find the scale factor we need to apply to $t\bar{t} + b\bar{b}$ simulation, we compare data and simulation in the high purity $t\bar{t} + b\bar{b}$ sample: two isolated leptons of opposite charge, large E_T^{miss}, and three b-tagged jets. The data/MC ratio is found to be 1.23 ± 0.10 (stat). Therefore, we scale the simulated event yield for events of the $t\bar{t} + b\bar{b}$. It is noted that this correction has applied to the dijet mass template after $t\bar{t}$ kinematic fit.

Since we perform a shape analysis for the search, having a smooth shape is very important. The backgrounds including at least one boson in the 3 b-tag region are estimated in simulation, however the simulation used to estimate these backgrounds suffer from low statistics when requiring 3 b-tagged jets. For this reason the non-top background estimation in the 3 b-tag signal region is done by applying the tagging efficiency to the non-tagged jets in the selected 2 b-tag events.

For background from multijet events where a non-prompt lepton is misidentified from a jet we use a data driven technique to estimate the contribution in the signal region. In this analysis we define a non-prompt lepton as any lepton that does not decay from a W or Z boson. For the misidentified lepton background the shape of the signal kinematics is obtained using signal-like events in the data, except the relative isolation (Iso_{rel}) of a lepton is between 0.15–0.3. Background events estimated from simulation samples ($t\bar{t}$ and non-top bacgkrounds) are subtracted from data for this multijet event estimation. To correct for the difference in normalisation of events in the signal region with an isolated and anti-isolated lepton a scale factor is applied to the anti-isolated sample. This scale factor is defined as the ratio of the number of events with a single isolated lepton versus a single anti-isolated lepton and is determined using a sample of data events orthogonal to the signal region ($E_T^{miss} < 20$ GeV). The scale factor used for estimating the misidentified lepton background in signal region were obtained in 2 b-tagged events, and applied to the QCD estimation in both the 2 and 3 b-tagged selections. Kinematic distributions for the multijet background are obtained by applying the scale factor to events with an anti-isolated leptons with $E_T^{miss} > 20$ GeV. The same technique to estimate the multijet background was used previously in the $H^+ \rightarrow c\bar{s}$ search [27].

Selected event yields are listed in Tables 2 and 3 for the electron and muon channels. Lepton and jet p_T distributions for data and background-only in the 2b-tag category are shown in Figure 2, and 3 b-tag signal region observable kinematic distributions are compared in Figure 3 for e+jets and μ+jets selection together. The comparison shows a good agreement of data and background predictions.

Table 2: Event yields with the e+jets selection from simulation and data corresponding to 19.7 fb^{-1} at $\sqrt{s}$ = 8 TeV. The correction to the $t\bar{t}$ simulation in the 3 b-tag region is not applied here.

e+jets	1b-tag	2b-tag	3b-tag
$t\bar{t}$+jets	69289 ± 83	43592 ± 63	4007 ± 19
QCD multijet	6187 ± 87	1116 ± 33	82 ± 8
Single Top	4069 ± 43	1882 ± 28	147 ± 8
W/Z+jets	10351 ± 368	1098 ± 114	79 ± 20
WW/WZ/ZZ	290 ± 5	56 ± 2	5.4 ± 0.4
$t\bar{t}$+W/Z/H	279 ± 2	169 ± 2	35 ± 1
Total Bkgd	90464 ± 389	47911 ± 137	4355 ± 30
Observed	92877	50542	4848

Table 3: Event yields with the μ+jets selection from simulation and data corresponding to 19.7 fb^{-1} at $\sqrt{s}$ = 8 TeV. The correction to the $t\bar{t}$ simulation i n the 3 b-tag region is not applied here.

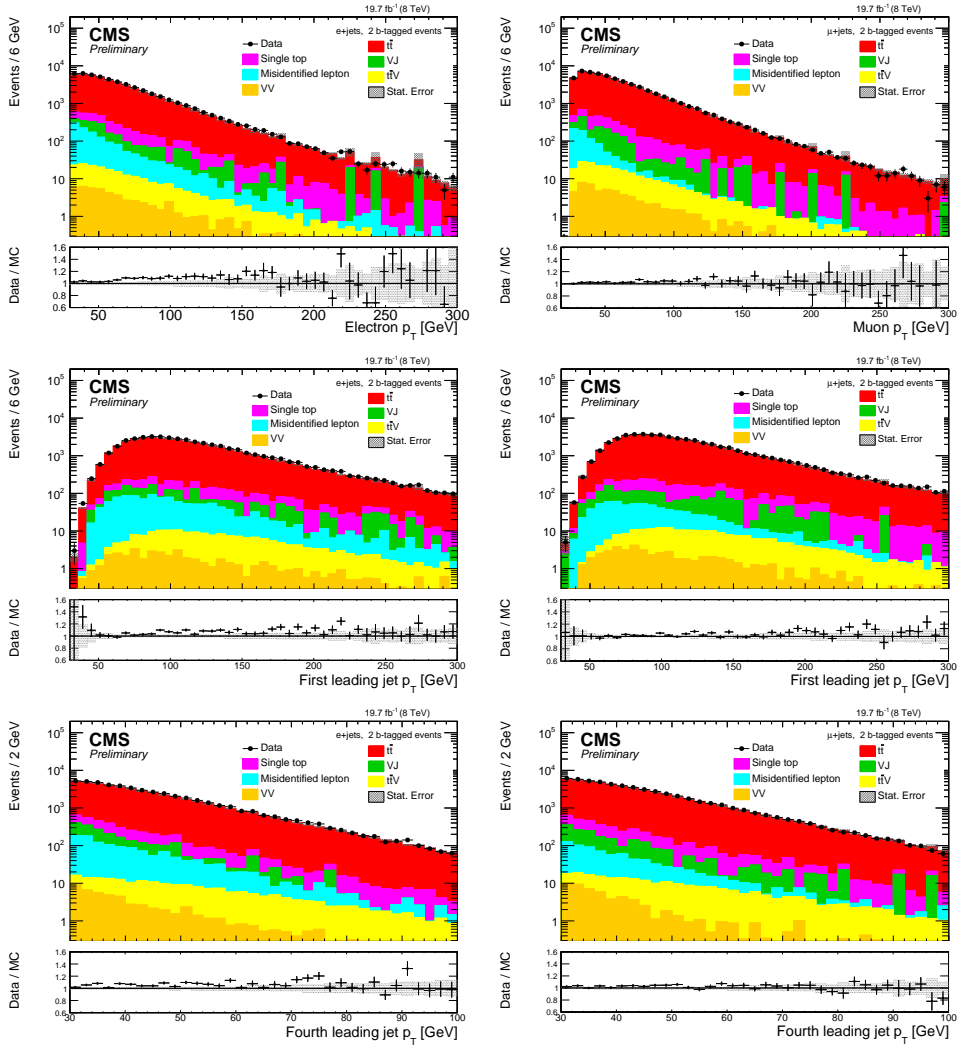| μ+jets	1 b-tag	2 b-tag	3 b-tag
$t\bar{t}$+jets	81622 ± 91	51823 ± 69	4755 ± 21
QCD multijet	2446 ± 42	597 ± 17	51 ± 5
Single Top	4829 ± 47	2212 ± 30	169 ± 8
W/Z+jets	11982 ± 417	1306 ± 127	64 ± 12
WW/WZ/ZZ	330 ± 6	62 ± 2	7 ± 1
$t\bar{t}$+W/Z/H	322 ± 2	195 ± 2	41 ± 1
Total Bkgd	101531 ± 431	56195 ± 149	5087 ± 26
Observed	102404	57593	5754

Figure 2: Lepton and jet p_T distributions for data and background-only in the 2b-tag category: (top left) electron; (top-right) muon; the four bottom plots are for the four leading jets. The data-driven correction to the $t\bar{t}$ simulation in the 3 b-tag region is not applied in these plots.
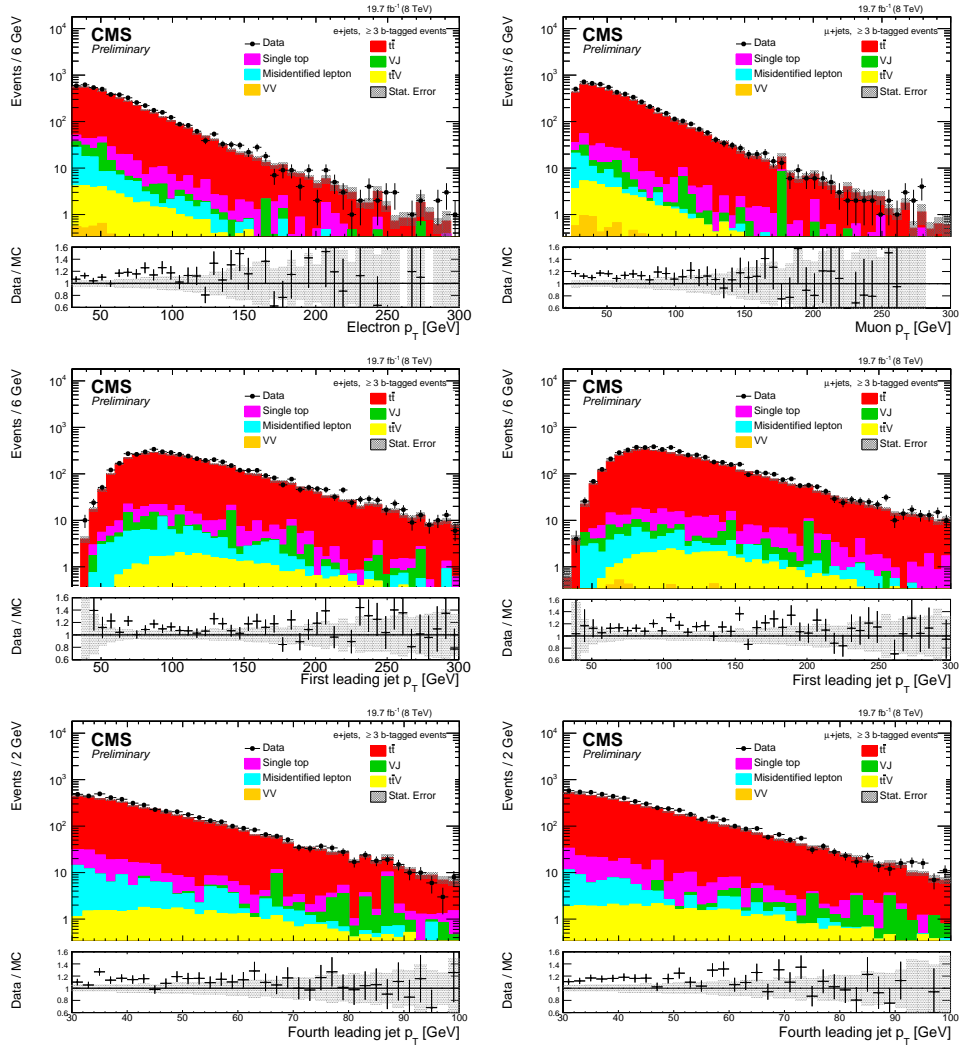
Figure 3: Lepton and jet p_T distributions for data and background-only in the 3b-tag category: (top left) electron; (top-right) muon; the four bottom plots are for the four leading jets.

6 Top Quark Specific Correction to Jets

The search for a charged Higgs boson is performed using the dijet mass distributions for a pair of jets selected as the best match for a $H^+ \rightarrow c\bar{b}$ decay. Therefore, it is important to achieve a good dijet mass resolution. Standard jet energy corrections bring the jet energy to particle level. In this analysis, we introduce additional parton-specific jet energy corrections so that the corrected jet energy matches closer to the energy of the primary quark of a specific flavour (b, c, and light quarks u/d/s). The assignment of jets to specific quarks arising in $tt \rightarrow \ell \nu + 4jets$ decays (and selection of a candidate pair to be associated with a potential Higgs boson decay) is performed by the kinematic fitter to be described in the next section. The jet-parton p_T response function f is defined in Equation 1 comparing the matched parton p_T with the reconstructed jet p_T.

$$f = \frac{p_T(\text{parton}) - p_T(\text{jet})}{p_T(\text{jet})} \tag{1}$$

The response function is referred to as a top quark specific (TS) correction. Among the four partons generated in the lepton+jets channel SM $t\bar{t}$ events, two of them are decay products of a W and the other two are b and $\bar{b}$ quarks from t and $\bar{t}$, respectively. The matching between a parton and reconstructed jet is done based on a matching with $\Delta R < 0.3$. When more than one jet is matched to a parton, this event is not used. The jet response function is fit with a function of p_T as shown in Equation 2 for each parton flavour (b, c, and u/d/s), and is shown in Figure 4.

$$f(p_T) = a + b \times \sqrt{p_T} + \frac{c}{p_T} + d \times p_T. \tag{2}$$

This response function fit is repeated for each jet η regions. In addition, for the p_T response of a jet matched to a b quark, a constraint on $|\Delta p_T(\text{parton}, \text{jet})| < 25$ GeV is applied to prevent over-correction.
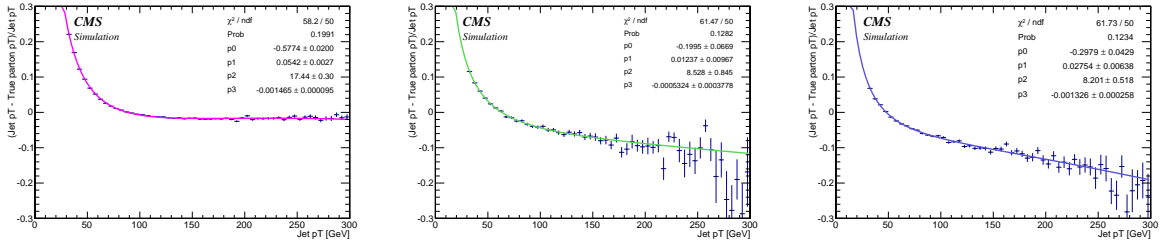

Figure 4: Jet p_T response as a function of reconstructed p_T for a b quark jet, c quark jet, and light-flavour jets in $|\eta| < 0.174$.

With the TS correction applied, the corrected jet p_T should be closer to the corresponding parton p_T. Thereby, the p_T of the TS corrected jets are compared with the original matching parton in selected p_T and η bins. Corrected p_T response distributions, p_T(TS-corrected jet - p_T(parton), are shown for the case of the $|\eta| < 0.174$ in Figure 5. The jet energy resolution after the TS correction is obtained from the width of Gaussian fit on the residual distribution in each p_T and η region. The resolution width in each $|\eta|$ region is again parameterized as a function of p_T using the Equation 2 and used in the kinematic fit as described in the Sec. refsec:ttres.

Figure 6 compares the invariant mass distributions with and without the TS corrections for the dijet mass of a boson and for the hadronic side top quark masses, M(bq$\bar{q}$) and M(bc$\bar{b}$). The jets
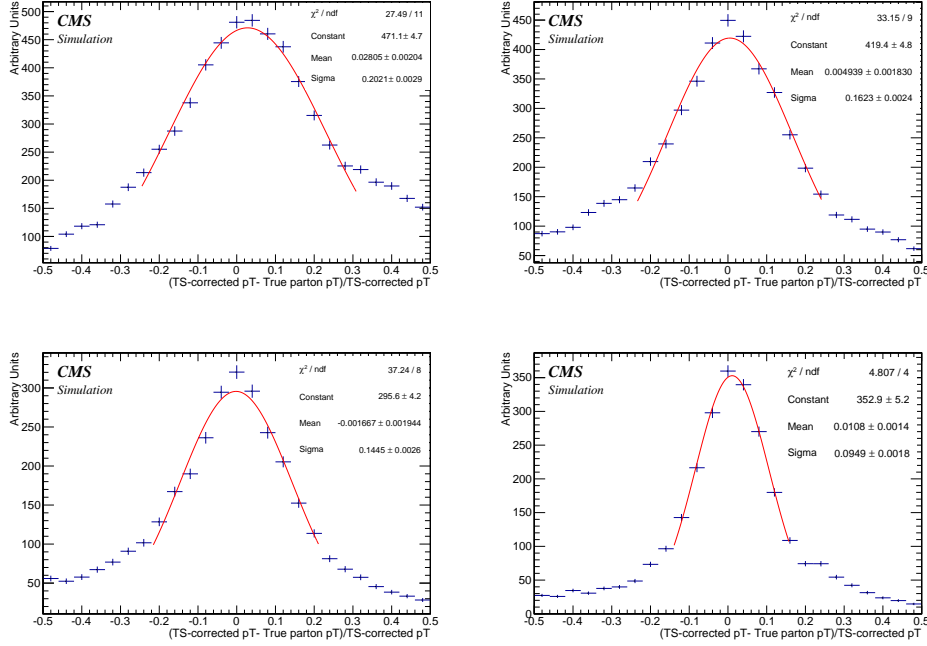
Figure 5: Corrected p_{T} response distributions for b quark jets for $|\eta| < 0.174$. From the top left, some selected plots for different p_{T} ranges: (50,60), (70,80), (90,100), and (150,300).

used in the Figure 6 are matched to the quarks from the SM $t\bar{t}$ events and from the H^+ signal samples, thereby the TS corrections are applied to those jets according to the matching quark's flavour. With the TS correction applied the mean value of the dijet mass distribution is closer to the true value, while the resolution is improved by 7~9 % in both samples.

7 $t\bar{t}$ Event Reconstruction

The resolution of the dijet invariant mass is improved further by using a kinematic fitter. The fitter is performed to find the best-matched assignment of four jets to the four quarks in the semi-leptonic decays of $t\bar{t}$. In the selected events, only four leading jets are assumed to be from the tree level partons and used for the $t\bar{t}$ reconstruction. The TS correction is applied to those selected jets in the kinematic fitter based on its assigned parton flavor. For example, a jet which is assigned to be the b quark from the top quark decay is corrected with the b flavour TS correction for a given jet p_{T}. The minimization χ^2 function used for the H^+ search is defined as

$$
\begin{aligned}
\chi^2 \;=\; & \sum_{i=l,4jets} \frac{(p_{\mathrm{T}}^{i,fit} - p_{\mathrm{T}}^{i,meas})^2}{\sigma_i^{\,2}} + \sum_{j=x,y} \frac{(p_j^{NE,fit} - p_j^{NE,meas})^2}{\sigma_{NE}^{\,2}} \\
& + \; \frac{(M_{l\nu} - M_W)^2}{\Gamma_W^{\,2}} + \frac{(M_{bl\nu} - M_t)^2}{\Gamma_t^{\,2}} + \frac{(M_{bbc} - M_t)^2}{\Gamma_t^{\,2}}.
\end{aligned}
\tag{3}
$$

While constraining the invariant masses of the leptonic W, and both the leptonic and hadronic top quarks to the true values in simulation, 80.4 GeV and 172.5 GeV respectively, the `MINUIT` fitter runs to find the best jet to parton assignment with the smallest χ^2 by varying the p_{T} of leading four jets and lepton, and the non-clustered jet energy (NE) accordingly. The lepton
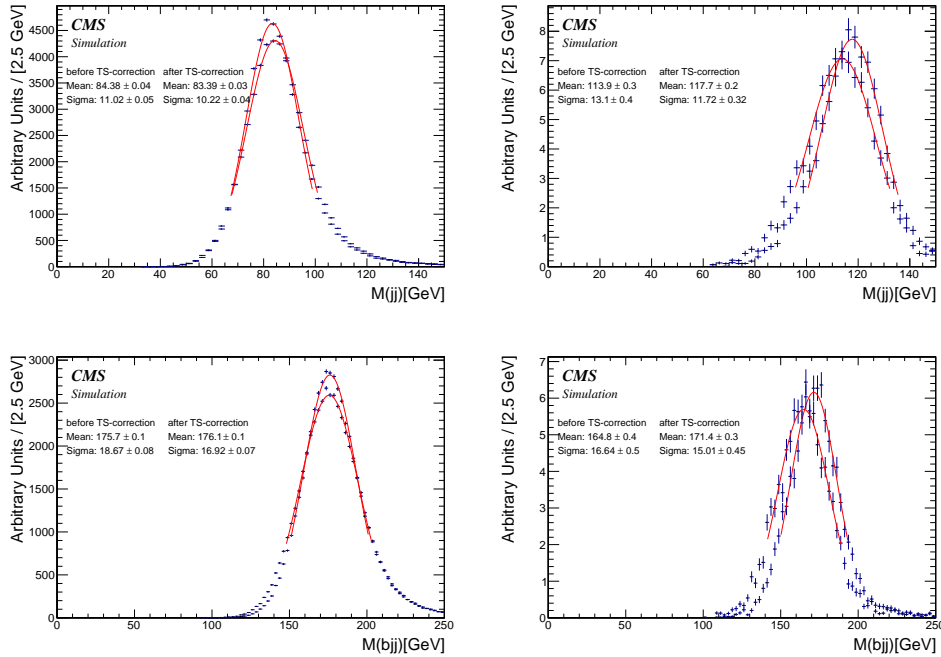
Figure 6: Top plots show M(jj) distribution before and after the TS correction for SM t$\bar{\text{t}}$ (top left) and for H$^+$(120) signal (top right), while the bottom plots are M(bq$\bar{\text{q}}$) for t$\bar{\text{t}}$ (bottom left) and M(bc$\bar{\text{b}}$) for 120 H$^+$(120) signal (bottom right)

.

p_T is varied within its uncertainty. Input jets to the fitter are TS-corrected for each jet-parton combination, then the corresponding resolution of the TS correction is used for as the jet p_T uncertainty. The non-clustered energy is firstly estimated by

$$NE_{x,y} = -\text{p}_{x,y}(\text{lepton}) - \sum_{\text{jets}(\text{p}_T > 10\,\text{GeV})} \text{p}_{x,y} - \text{E}_T^{\text{miss}}{}_{x,y}, \tag{4}$$

then varies in the fitter. Non-clustered energy is not very well understood, thereby relatively large uncertainty (50%) is used. The E_T^{miss} is then derived from the NE fit output using the relationship shown in Equation 4.

In two b-jets event, each b-tagged jet is assigned to the two top quark decays, so that the dijet mass is reconstructed from two un-tagged jets. When an event has three b-tagged jets, any two b-tagged jets are assigned to two top-b-quarks and one remaining b-tagged jet is assigned to either W/H$^+$ based on the minimum χ^2 for the low mass H$^+$ ($\leq$ 120 GeV). However, for a higher mass H$^+$ (130 - 150 GeV) that has decayed from a top quark, the accompanying b quark becomes softer. Figure 7 compares the generated p_T distribution of the top-b-quark in H$^+$ samples with that from the SM t$\bar{\text{t}}$ sample. Since there are no constraints on the dijet mass, the fitter confuses the b-jet assignment between two b-quarks from the same hadronic top quark, which degraded the dijet mass resolution worse. Subsequently among two b-tagged jets from the process t $\rightarrow$ H$^+$b $\rightarrow$ H$^+\bar{\text{b}}$b, the softer p_T jet is assigned to the top-b-quark in the fitter.

To mitigate somewhat the problem of wrong assignments, two goodness cuts are applied in selecting the best-matched assignment rather than imposing a cut on χ^2 as shown below. These cuts help preventing the occurence of a wrong jet-parton assignment which result in a small χ^2. The efficiency of these goodness cuts is estimated to be about 50% for SM t$\bar{\text{t}}$ and 60% for the H$^+$ signal t$\bar{\text{t}}$ sample in $\geq$ 3 b-tags region.
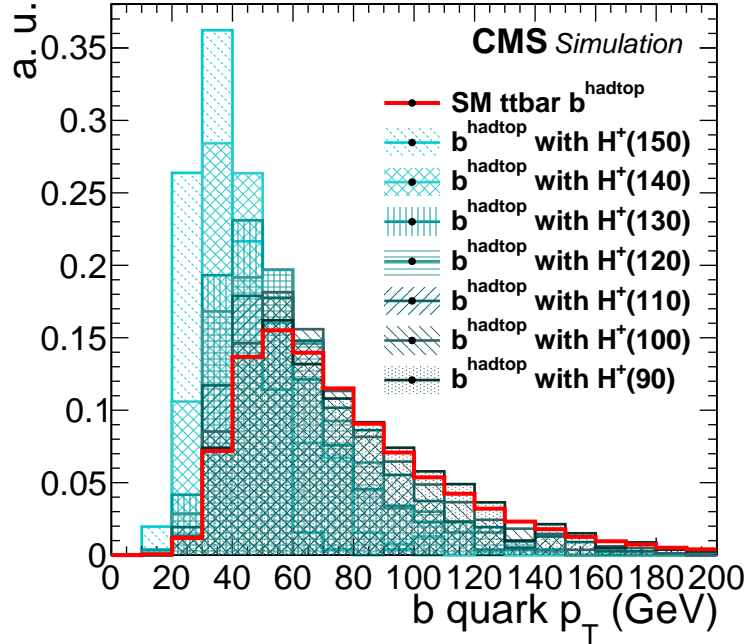
Figure 7: p_{T} distribution of the top-b-parton in the hadronic side top quark. The b-quark p_{T} distribution in the SM $t\bar{t}$ sample (red) is compared with the H^+ signal $t\bar{t}$ sample with $M(H^+)$ = 90, 100, 110, 120, 130, 140, and 150 GeV.

- $|p_{\mathrm{T}}^{\mathrm{in}} - p_{\mathrm{T}}^{\mathrm{fitted}}| < 20$ GeV for each jet,
- M(hadronic top quark) (before fit) < 200 GeV.

The obtained dijet mass distributions (i.e., the mass of the two non b-tagged jets in the 2 b-tagged region) from the $t\bar{t}$ reconstruction fitter are shown in Figure 8. Figures 9 and 10 show the dijet mass distributions in the 3b-tagged region as obtained with the low and high mass fitters, respectively. In all these plots the $t\bar{t}$ background is scaled down due to the presence of signal, according to the branching ratio, B(t$\rightarrow$H$^+$b). Additionally the $t\bar{t}$ similation is scaled up by a factor of 1.23 in the 3 b-tag region as discussed in Section 5. The signals shown correspond to M(H$^+$)=110/140 GeV and B=0.2 (Fig. 8), M(H$^+$)=110 and B=0.05 (Fig. 9), and M(H$^+$)=140 and B=0.05 (Fig. 10).

8   Systematic Uncertainties

In this analysis, we use both 2 b-tag and 3 b-tag events sample. The sample with 2 b-tag events are dominated by background contributions, whereas signal events are mostly in the 3 b-tag region. Thus many common systematics between 2 b-tag and 3 b-tag events can be constrained using the high-statistics of the 2 b-tags data.

Effect on the analysis templates from systematic sources appears in two aspects. The first one is related to the overall rate of signal and background contributions, while the second one affects the shape of the dijet mass distribution. In several cases the systematic source changes both rate and kinematic shape. For the systematic uncertainty estimation, we use the top quark analysis group guideline and systematic samples, which are well described in the Ref. [43].
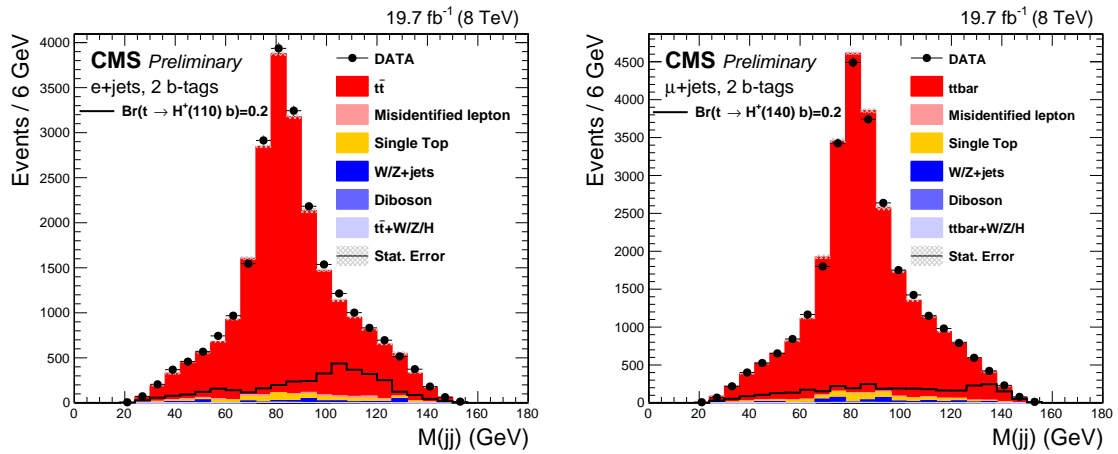
Figure 8: Dijet mass distribution MC background stack in the two b-tagged jets events in e+jets (left) and μ+jets (right) channel. Dijet mass distribution of H$^+$ signal sample with H$^+$ mass 110 GeV (140 GeV) are compared on top of the background stack.
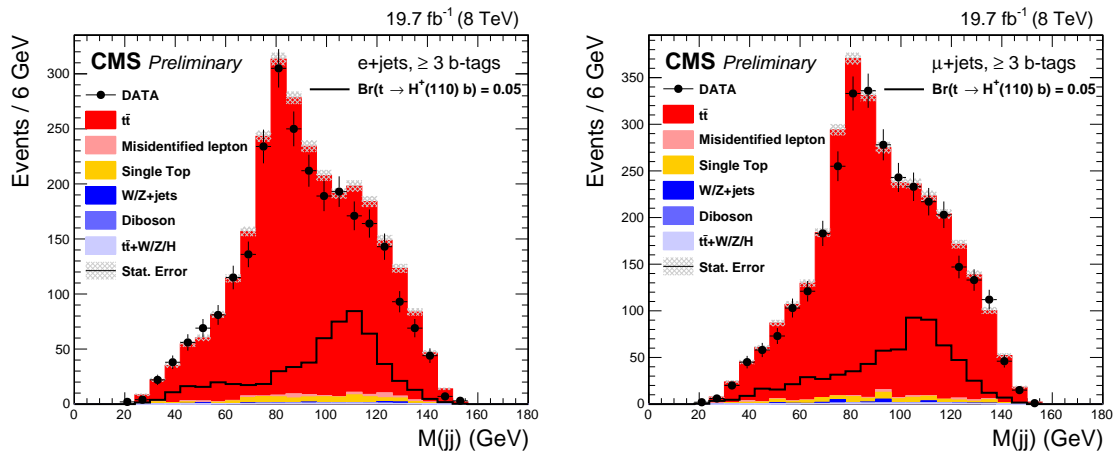

Figure 9: Dijet mass distribution MC background stack in the three b-tagged jets events in e+jets (left) and μ+jets (right) channel with the normal fitter. Dijet mass distribution of H$^+$ signal sample with H$^+$ mass of 110 GeV is compared on top of the background stack.
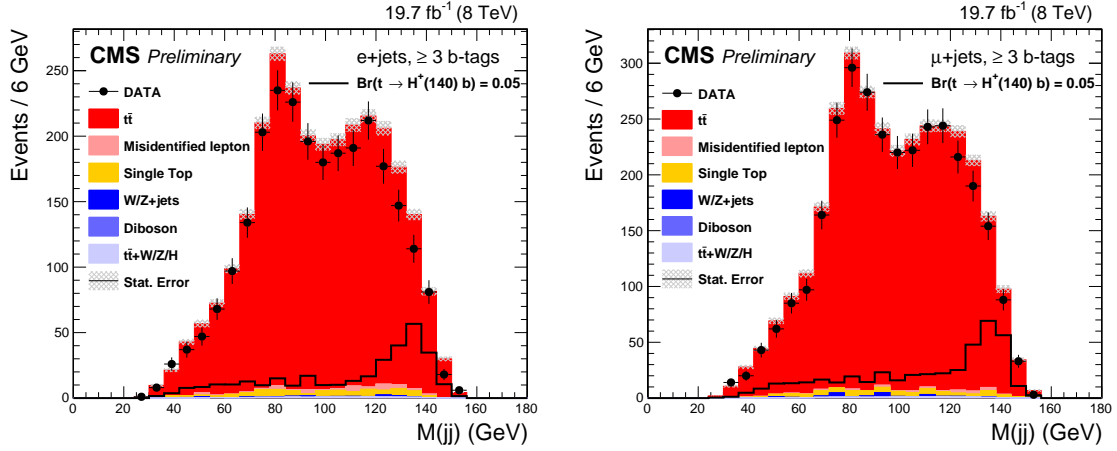
Figure 10: Dijet mass distribution MC background stack in the three b-tagged jets events in e+jets(left) and μ+jets(right) channel with the high mass fitter. Dijet mass distribution of H$^+$ signal sample with H$^+$ mass 140 GeV is compared on top of the background stack.

.

The considered sources of uncertainties summarized in Table 4 and more details follow:

Table 4: Summary of the systematic uncertainties in the search for a charged Higgs boson covering both the μ+jet and e+jet channels. For cases where the uncertainties in the μ+jet and e+jet channels differ, range is given. Rate uncertainties for the H$^\pm$ signal, t$\bar{\text{t}}$, non-t$\bar{\text{t}}$ are listed for the 2 b-tag and 3 b-tag selections, and the uncertainties marked with (s) are used for shape systematic uncertainties.

Source of uncertainty	signal ($m_H = 120$)		t$\bar{\text{t}}$		non-t$\bar{\text{t}}$		QCD multijet	
	2 b-tag	3 b-tag	2 b-tag	3 b-tag	2 b-tag	3 b-tag	2 b-tag	3 b-tag
t$\bar{\text{t}}$ cross section	6.5	20	6.5	20				
Top quark mass	5 (s)	5 (s)	5 (s)	5 (s)				
t$\bar{\text{t}}$ p_T reweighting	(s)	(s)	(s)	(s)				
NLO-vs-LO shape								
(Powheg-vs-MadGraph)	8.5–9.0 (s)	7.6–8.8 (s)	8.3–8.5 (s)	8.0 (s)				
PYTHIA–MADGRAPH p_T(t$\bar{\text{t}}$) difference	(s)	(s)						
ME-PS matching			0.6–0.8 (s)	0.8–1.4 (s)				
Renormalization and factorization scales	4.0–4.2 (s)	6.8–7.2 (s)	1.3–1.7 (s)	1.3–2.0 (s)				
Jet energy scale (JES)	4.6–5.3 (s)	5.0–5.9 (s)	3.4 (s)	3.3 (s)	7.5–9.6 (s)	0.9–2.8 (s)		
Flavour-dependent JES (b quark)	0.3–0.4 (s)	0.2–0.6 (s)	0.1 (s)	9.0 (s)	0.1–0.7 (s)	0.5–0.9 (s)		
Flavour-dependent JES (udsc,g)	0.9–1.2 (s)	0.4–0.6 (s)	1.0 (s)	9.0 (s)	3.1–4.1 (s)	1.1–1.8 (s)		
Jet energy resolution	0.1–0.2 (s)	0.2–0.8 (s)	0.3 (s)	0.4 (s)	1.1 (s)	1.5 (s)		
B-tag scale factor for b/c quark jets	1.2–2.1	5.6–5.8	3.6	5.7	2.9–3.0	4.0–4.4		
Mis-tag scale factor for light quark jets	0.1–0.2	0.2–0.7	0.2	0.3–0.7	0.7–1.3	0.3–0.4		
Pileup reweighting	≈ 0.5							
Electron scale factor (e+jets)	2.0							
Muon scale factor (μ+jets)	2.0							
Luminosity	2.6							
Data driven prediction							Shift anti-Iso$_{rel}$ region (s)	

- t$\bar{\text{t}}$ **cross section:** The theoretical value of the t$\bar{\text{t}}$ cross section is used to estimate the backgrounds of the SM t$\bar{\text{t}}$ which has an uncertainty of 6.5%. The calculation is done at next-to-next-to leading order (NNLO) in QCD including resummation of next-to-next-to-leading logarithmic (NNLL) of the soft gluon terms [44]. However this uncertainty may not be sufficient in the 3 b-tags region, where there can be an additional uncertainty in the modelling of additional $b\bar{b}$ production. As described in Section 5, the t$\bar{\text{t}}$ +bb contribution to the t$\bar{\text{t}}$ background in the 3b-tag category is scaled up by factor of 1.23, derived from comparing data and simulation in a control region. Since the origin of this data-vs-simulation difference is not yet understood, we assign 20% uncertainty on the entire t$\bar{\text{t}}$ background in the 3b-tag category.

- **Top quark mass:** Two $t\bar{t}$ simulation samples generated with alternative top quark masses, 171.5 GeV and 173.5 GeV, are used to assess the uncertainty in the M(jj) template distributions and event yields associated with the uncertainty in the top quark mass.

- **$t\bar{t}$ p_T-reweighting:** The p_T spectrum of individual top quarks observed in data [45] was found to be softer than the NNLO QCD predictions [46, 47]. Event-by-event weights have been derived by CMS top quark analysis group, then applied to the $t\bar{t}$ simulation. The difference in the M(jj) templates obtained with and without reweighting is taken as a systematic uncertainty.

- **NLO-vs-LO shape:** To estimate the uncertainty due to the missing NLO contributions, we use Powheg (NLO) to simulate an alternative $t\bar{t}$ sample. The difference between the M(jj) templates obtained with MadGraph and Powheg (Figure 11) is taken as a shape uncertainty.

- **PYTHIA–MADGRAPH $p_T(t\bar{t})$ difference:** The H$^+$ signal sample is generated by PYTHIA while the SM $t\bar{t}$ sample was done by MADGRAPH. The difference between two generators appear in the different peaks in the $p_T(t\bar{t})$ spectrum at the generate level. Effect on the dijet mass distribution is estimated by applying the event weight by $p_T(t\bar{t})$ shape from SM $t\bar{t}$ to that of H$^+$ signal $t\bar{t}$, then added to the shape systematic uncertainty.

- **ME-PS matching:** In the $t\bar{t}$ simulation sample, matching threshold that interfaces the matrix element (MADGRAPH) to the parton-showering (PYTHIA) is shifted up/down as desribed in Ref. [43].

- **Renormalization and factorization scales (Q^2):** The uncertainty on the M(jj) template of $t\bar{t}$ background due to missing beyond-LO terms is estimated by varying the renormalization and factorization scale by the conventional factor of 2 up and down. This can be a double counting of the NLO-vs-LO shape uncertainty, however we take a conservative estimation on uncertainties.

- **Jet energy scale (JES):** The JES uncertainty is one of the most significant sources of uncertainty in this analysis. This uncertainty affects both the event yield and the mass template shapes. The JES uncertainty is evaluated as a function of jet p_T and η [48].

- **Flavour dependent JES:** The jet energy response may not be same for different parton flavour. An additional uncertainty for different parton flavour is studied along with the jet energy corrections [48]. In order to separate the effect by parton flavour, the uncertainties are estimated separately by $\pm 1\sigma$ shift of only b-quark jets and by $\pm 1\sigma$ shift for other jets. This uncertainty also takes into account the difference in the hadronization processes given by the difference from PYTHIA to HERWIG.

- **Jet energy resolution (JER):** Previous measurements of jet energy resolution in data have indicated that it is about 10% worse than in the simulation [48]. The resolution in simulated events is therefore degraded accordingly to match the data. Based on the jet energy, the resolution for each jet is scaled up and down within its uncertainty.

- **B-tagging scale factor:** The b-tagging scale factor uncertainty has a large impact on event rates for signal and backgrounds. According to the b-tagging performance study for 2012 CMS data [49], the scale factor for mistag is $1.17 \pm 0.02(\text{stat.}) \pm 0.15(\text{syst.})$ and the for the b and c quarks it is assigned to be $0.953 \pm 0.012(\text{combined})$. We use same scale factor for b and c quarks but assigns doubled uncertainty for the c quark.

- **Pileup reweighting:** To estimate the uncertainties associated with pileup, the minimum-

bias pp cross section used in the minimum bias production used in the pileup reweighting procedure in simulation is varied up and down by 5%

- **Lepton identification/isolation/trigger scale factor:** For both e+jets and μ+jets channels, the uncertainty on the lepton identification and isolation efficiencies are estimated to be 0.2% (0.04%) for electron (muon). We assign an uncertainty of 2% on the rate by combining the identification and isolation scale factor uncertainties with the trigger scale factor uncertainty (0.5%/0.04% for electron/muon) [27].

- **Luminosity uncertainty:** The uncertainty on the luminosity measurement is given to be 2.6% by the Luminosity group [50].

- **Data driven multijet:** The uncertainty on data-driven multijet background is estimated by shifting anti-isolation region, which is defined by $0.15 < \text{Iso}_{\text{rel}} < 0.30$ of a selected lepton in the analysis. The dijet mass distributions for multijet uncertainty is obtained by (1) inverting the standard isolation cut ($\text{Iso}_{\text{rel}} > 0.1$ (0.12) for electron (muon)) and (2) using $0.2 < |\text{Iso}_{\text{rel}}| < 0.3$. The shape and rate are then re-evaluated for the non-$t\bar{t}$ background template using these two new shifted multijet contributions.
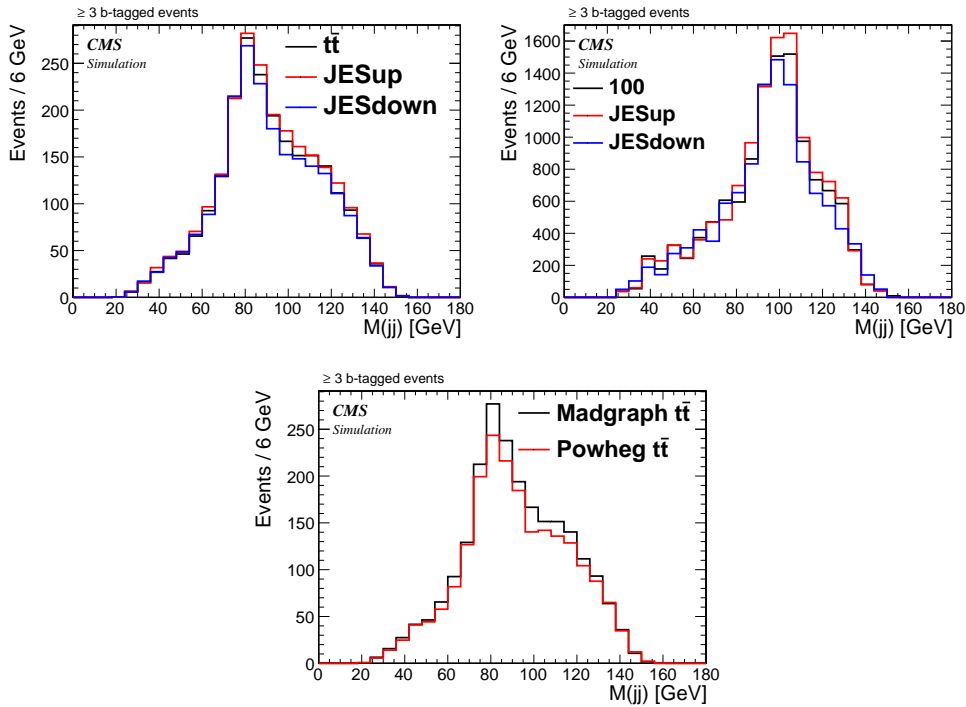

Figure 11: Comparison of dijet mass distribution using low mass fitter for the SM $t\bar{t}$ (left) and for charged Higgs boson signal at 100 GeV (right) in 3 b-tags e+jets channel: shifts due to jet energy scale: $t\bar{t}$ (top left), signal (top right), $t\bar{t}$ MC generator (bottom).

9   Results

`RooStat` [51] based statistics tools are used for this shape analysis. The observed data in the four signal regions (Figures 8 and 9 or Figures 8 and 10) are fitted using a Maximum Likelihood Fit (MLF) Method for the branching ratio B(t→H$^+$b), assuming B(H$^+ \to c\bar{b}$)=100%, using the binned M(jj) templates for background and signal. Expected number of events in a mass bin i

consists of

$$\mu_i = \mu_i(non-t\bar{t}) + (1-BR)^2 \times \mu_i(t\bar{t} \rightarrow WbW^-\bar{b}) + 2 \times BR \times (1-BR) \times \mu_i(t\bar{t} \rightarrow H^+bW^-\bar{b}), \quad (5)$$

whereas the BR is B(t→H$^+$b) and μ_i is the number of events in i-th bin mass templates for non-t$\bar{t}$ SM backgrounds, H$^+$, and SM t$\bar{t}$(W). These templates are normalized by the best MLF value in Fig. 12 and Fig. 13. Figure 12 shows the dijet mass distribution of the templates with observed data in 2 b-tagged region where the SM t$\bar{t}$ process is dominant. Figure 13 shows the 3 b-tagged region fit on data for the low H$^+$ mass fitter on the left and for high H$^+$ mass fitter on the right. Based on the fit on data, the t$\bar{t} \rightarrow$ H$^+$bH$^-\bar{b}$ contribution to the fit is neglected. The expected dijet mass distribution, assuming the H$^+$ signal is produced with the B(t→H$^+$b) equal to the expected limit, are compared in the same figures. Presence of the H$^+$ signal causes t$\bar{t} \rightarrow$ WbWb being decreased, which results in the event deficit in the 2 b-tagged region and an excess in the $\geq$ 3 b-tagged region.
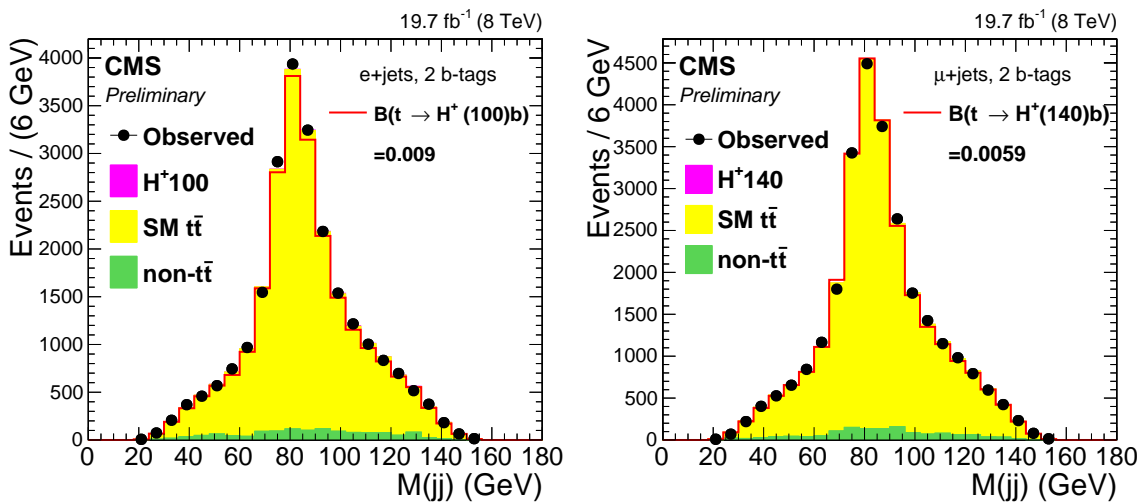

Figure 12: Dijet mass distribution MC stack in the two b-tagged jets events are fitted on the observed data by maximum likelihood fit in e+jets(left) and μ+jets(right) channel. The best branching ratio from the fit is written on the figure for a 100 GeV (left) and a 140 GeV (right) H$^+$ mass. Dijet mass distribution with injecting signal B(t→H$^+$b) equal to the expected limit is overlaid.

The best-fit values for B(t→H$^+$b) for all Higgs boson mass hypotheses are consistent with B=0. The upper 95% CL limits are obtained by setting $2 \ln \frac{L(data|B,\hat{\hat{\theta}}_B)}{L(data|\hat{B},\hat{\theta})} = 3.84$, where the denominator is the global likelihood maximum, while the numerator is the likelihood maximum at a given B. The results are shown in Figure 14. The limits with statistics uncertainty only are overlaid in the same plot to show the systematic effect on the limits. As the mass of the H$^+$ tends to the mass of the W, the limit obtained using all systematic uncertainties is found to be a factor of two larger than the limit obtained using the statistical uncertainty only. It implies that this analysis is seriously affected by the systematic uncertainties, however, this effect is diminished when the mass separation becomes clear at the high mass of the H$^+$. Combining both electron and muon channels, the 95% C.L. upper limits on B(t→H$^+$b) are obtained to be 0.4 to 1.1%.
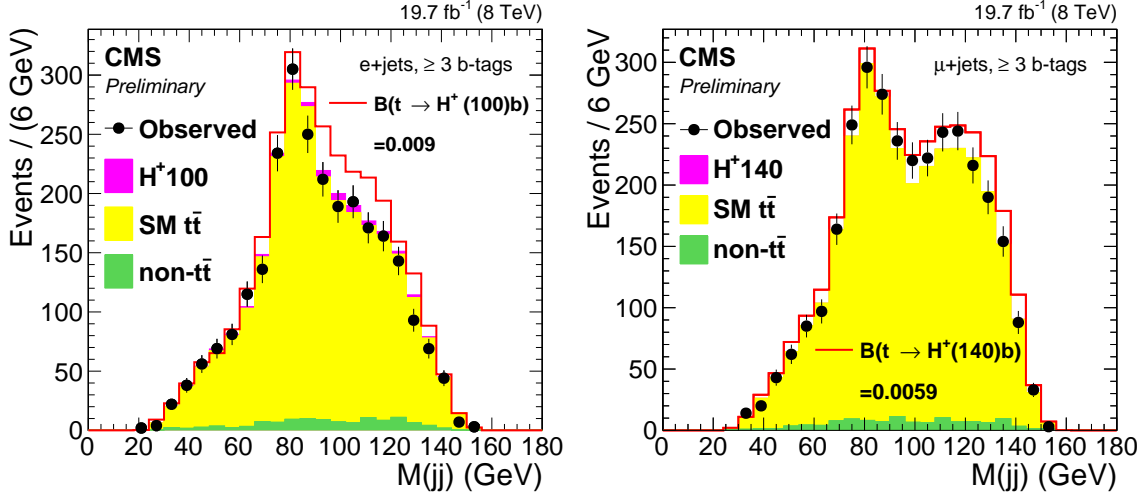
Figure 13: Dijet mass distribution MC stack in the at least three b-tagged jets events are fitted on the observed data by maximum likelihood fit in e+jets(left) and μ+jets(right) channel with the low (left) and high mass (right) fitter. Dijet mass distribution with injecting signal B(t→H$^+$b) equal to the expected limit is overlaid.

10   Summary

Results on the search for a light charged Higgs boson H$^+$ decaying to c$\bar{\text{b}}$ in top quark pair events using the CMS detector at the LHC are presented. The total dataset corresponds to 19.7 fb^{-1} of proton-proton collisions at $\sqrt{s}$ = 8 TeV. In t$\bar{\text{t}}$ decays, if one top quark decays to H$^+$b, instead of Wb, and the H$^+$ subsequently decays to c$\bar{\text{b}}$, while other top quark decays leptonically ($\bar{\text{t}} \to$ W$^-\bar{\text{b}} \to \ell\bar{\nu}\bar{\text{b}}$), the final state then consists of four jets (three b quark jets), one lepton (electron or muon), and missing energy: t$\bar{\text{t}} \to$ (H$^+$b)(W$^-\bar{\text{b}}$) $\to$ (c$\bar{\text{b}}$b)($\ell\bar{\nu}\bar{\text{b}}$). The main observable used in the analysis is an invariant mass of two jets, one of which is identified as a b quark jet. The dijet pair is selected from at least four jets in an event by a dedicated kinematic fitter. No signal for the presence of a charged Higgs boson is observed and upper limits are set at 95% confidence level on the branching ratio for t $\to$ H$^+$b from 1.1–0.4% for the charged Higgs boson mass in the range 90–150 GeV in the assumption of branching ratio of B(H$^+ \to$ c$\bar{\text{b}}$) = 100% for the first time.
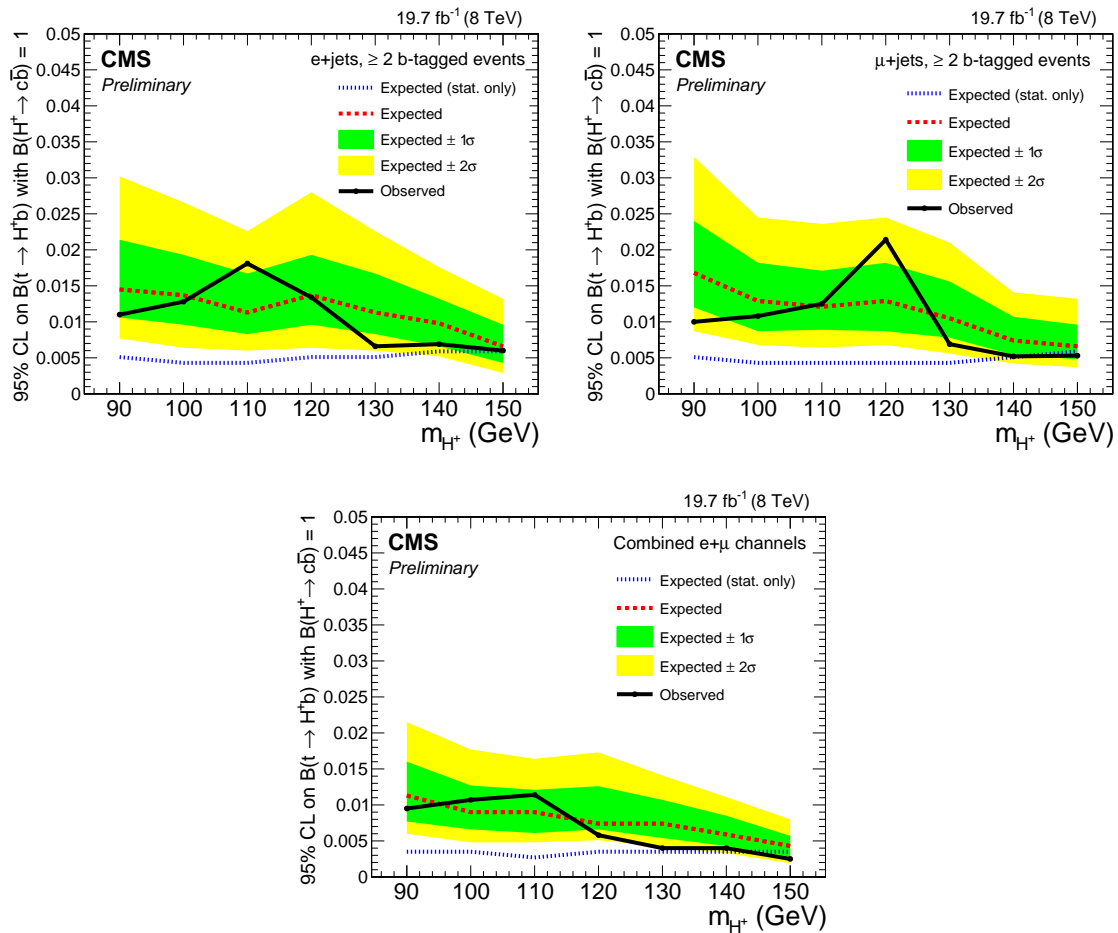
Figure 14: Observed upper limits on B(t→H$^+$b) with 95% C.L. are shown for electon channel (top left), muon channel (top right), and combined channel (bottom) with expected limts including all systematic uncertainties. The limits with statistical uncertainty only are overlaid in blue dots to show the effect of systematic uncertainties.

References

[1] CMS Collaboration, "Observation of a new boson at a mass of 125 GeV with the CMS experiment at the LHC", *Phys. Lett.* **B716** (2012) 30–61, `doi:10.1016/j.physletb.2012.08.021`, `arXiv:1207.7235`.

[2] ATLAS Collaboration, "Observation of a new particle in the search for the Standard Model Higgs boson with the ATLAS detector at the LHC", *Phys. Lett.* **B716** (2012) 1–29, `doi:10.1016/j.physletb.2012.08.020`, `arXiv:1207.7214`.

[3] CMS Collaboration, "Precise determination of the mass of the Higgs boson and tests of compatibility of its couplings with the standard model predictions using proton collisions at 7 and 8 TeV", *Eur. Phys. J.* **C75** (2015), no. 5, 212, `doi:10.1140/epjc/s10052-015-3351-7`, `arXiv:1412.8662`.

[4] ATLAS Collaboration, "Measurements of the Higgs boson production and decay rates and coupling strengths using pp collision data at $\sqrt{s} = 7$ and 8 TeV in the ATLAS experiment", *Eur. Phys. J.* **C76** (2016), no. 1, 6, `doi:10.1140/epjc/s10052-015-3769-y`, `arXiv:1507.04548`.

[5] ATLAS, CMS Collaboration, "Combined Measurement of the Higgs Boson Mass in pp Collisions at $\sqrt{s} = 7$ and 8 TeV with the ATLAS and CMS Experiments", *Phys. Rev. Lett.* **114** (2015) 191803, `doi:10.1103/PhysRevLett.114.191803`, `arXiv:1503.07589`.

[6] ATLAS, CMS Collaboration, "Measurements of the Higgs boson production and decay rates and constraints on its couplings from a combined ATLAS and CMS analysis of the LHC pp collision data at $\sqrt{s} = 7$ and 8 TeV", `arXiv:1606.02266`.

[7] S. L. Glashow, "Partial Symmetries of Weak Interactions", *Nucl. Phys.* **22** (1961) 579–588, `doi:10.1016/0029-5582(61)90469-2`.

[8] S. Weinberg, "A Model of Leptons", *Phys. Rev. Lett.* **19** (1967) 1264–1266, `doi:10.1103/PhysRevLett.19.1264`.

[9] A. Salam, "Weak and Electromagnetic Interactions", *Conf. Proc.* **C680519** (1968) 367–377.

[10] F. Englert and R. Brout, "Broken Symmetry and the Mass of Gauge Vector Mesons", *Phys. Rev. Lett.* **13** (1964) 321–323, `doi:10.1103/PhysRevLett.13.321`.

[11] P. W. Higgs, "Broken symmetries, massless particles and gauge fields", *Phys. Lett.* **12** (1964) 132–133, `doi:10.1016/0031-9163(64)91136-9`.

[12] P. W. Higgs, "Broken Symmetries and the Masses of Gauge Bosons", *Phys. Rev. Lett.* **13** (1964) 508–509, `doi:10.1103/PhysRevLett.13.508`.

[13] G. S. Guralnik, C. R. Hagen, and T. W. B. Kibble, "Global Conservation Laws and Massless Particles", *Phys. Rev. Lett.* **13** (1964) 585–587, `doi:10.1103/PhysRevLett.13.585`.

[14] P. W. Higgs, "Spontaneous Symmetry Breakdown without Massless Bosons", *Phys. Rev.* **145** (1966) 1156–1163, `doi:10.1103/PhysRev.145.1156`.

[15] T. W. B. Kibble, "Symmetry breaking in nonAbelian gauge theories", *Phys. Rev.* **155** (1967) 1554–1561, `doi:10.1103/PhysRev.155.1554`.

[16] J. F. Gunion, S. Dawson, H. E. Haber, and G. L. Kane, "The Higgs hunter's guide", volume 80. Brookhaven Nat. Lab., Upton, NY, 1989. In the second printing (1990) by Perseus Books in the collection Frontiers in physics, no 80, a number of errors and omissions are corrected and the references at the end of each chapter are updated. A paperback reprint of the 1990 edition has been published in 2000.

[17] G. C. Branco et al., "Theory and phenomenology of two-Higgs-doublet models", *Phys. Rept.* **516** (2012) 1–102, `doi:10.1016/j.physrep.2012.02.002`, `arXiv:1106.0034`.

[18] E. A. Paschos, "Diagonal Neutral Currents", *Phys. Rev.* **D15** (1977) 1966, `doi:10.1103/PhysRevD.15.1966`.

[19] S. L. Glashow and S. Weinberg, "Natural Conservation Laws for Neutral Currents", *Phys. Rev.* **D15** (1977) 1958, `doi:10.1103/PhysRevD.15.1958`.

[20] CDF Collaboration, "Search for charged Higgs bosons from top quark decays in $p\bar{p}$ collisions at $\sqrt{s} = 1.96$-TeV.", *Phys. Rev. Lett.* **96** (2006) 042003, `doi:10.1103/PhysRevLett.96.042003`, `arXiv:hep-ex/0510065`.

[21] D0 Collaboration, "Search for charged Higgs bosons in decays of top quarks", *Phys. Rev.* **D80** (2009) 051107, `doi:10.1103/PhysRevD.80.051107`, `arXiv:0906.5326`.

[22] CMS Collaboration, "Search for a light charged Higgs boson in top quark decays in pp collisions at $\sqrt{s} = 7$ TeV", *JHEP* **07** (2012) 143, `doi:10.1007/JHEP07(2012)143`, `arXiv:1205.5736`.

[23] ATLAS Collaboration, "Search for charged Higgs bosons decaying via $H^{\pm} \to \tau^{\pm}\nu$ in fully hadronic final states using pp collision data at $\sqrt{s} = 8$ TeV with the ATLAS detector", *JHEP* **03** (2015) 088, `doi:10.1007/JHEP03(2015)088`, `arXiv:1412.6663`.

[24] ATLAS Collaboration, "Search for charged Higgs bosons decaying via $H^{+} \to \tau\nu$ in top quark pair events using pp collision data at $\sqrt{s} = 7$ TeV with the ATLAS detector", *JHEP* **06** (2012) 039, `doi:10.1007/JHEP06(2012)039`, `arXiv:1204.2760`.

[25] CDF Collaboration, "Search for charged Higgs bosons in decays of top quarks in p anti-p collisions at s**(1/2) = 1.96 TeV", *Phys. Rev. Lett.* **103** (2009) 101803, `doi:10.1103/PhysRevLett.103.101803`, `arXiv:0907.1269`.

[26] D0 Collaboration, "Search for Charged Higgs Bosons in Top Quark Decays", *Phys. Lett.* **B682** (2009) 278–286, `doi:10.1016/j.physletb.2009.11.016`, `arXiv:0908.1811`.

[27] CMS Collaboration, "Search for a light charged Higgs boson decaying to $c\bar{s}$ in pp collisions at $\sqrt{s} = 8$ TeV", *JHEP* **12** (2015) 178, `doi:10.1007/JHEP12(2015)178`, `arXiv:1510.04252`.

[28] ATLAS Collaboration, "Search for a light charged Higgs boson in the decay channel $H^{+} \to c\bar{s}$ in $t\bar{t}$ events using pp collisions at $\sqrt{s} = 7$ TeV with the ATLAS detector", *Eur. Phys. J.* **C73** (2013), no. 6, 2465, `doi:10.1140/epjc/s10052-013-2465-z`, `arXiv:1302.3694`.

[29] M. Aoki, S. Kanemura, K. Tsumura, and K. Yagyu, "Models of Yukawa interaction in the two Higgs doublet model, and their collider phenomenology", *Phys. Rev.* **D80** (2009) 015017, `doi:10.1103/PhysRevD.80.015017`, `arXiv:0902.4665`.

[30] H. E. Logan and D. MacLennan, "Charged Higgs phenomenology in the flipped two Higgs doublet model", *Phys. Rev.* **D81** (2010) 075016, `doi:10.1103/PhysRevD.81.075016`, `arXiv:1002.4916`.

[31] CMS Collaboration, "The CMS experiment at the CERN LHC", *JINST* **3** (2008) S08004, `doi:10.1088/1748-0221/3/08/S08004`.

[32] CMS Collaboration, "Commissioning of the Particle-Flow reconstruction in Minimum-Bias and Jet Events from pp Collisions at 7 TeV", Technical Report CMS-PAS-PFT-10-002, CERN, Geneva, 2010.

[33] M. Cacciari, G. P. Salam, and G. Soyez, "The Anti-k(t) jet clustering algorithm", *JHEP* **0804** (2008) 063, `doi:10.1088/1126-6708/2008/04/063`, `arXiv:0802.1189`.

[34] CMS Collaboration, "Jet energy scale and resolution in the CMS experiment in pp collisions at 8 TeV", `arXiv:1607.03663`.

[35] T. Sjostrand, S. Mrenna, and P. Z. Skands, "PYTHIA 6.4 Physics and Manual", *JHEP* **05** (2006) 026, `doi:10.1088/1126-6708/2006/05/026`, `arXiv:hep-ph/0603175`.

[36] J. Alwall et al., "MadGraph 5 : Going Beyond", *JHEP* **06** (2011) 128, `doi:10.1007/JHEP06(2011)128`, `arXiv:1106.0522`.

[37] S. Alioli, P. Nason, C. Oleari, and E. Re, "A general framework for implementing NLO calculations in shower Monte Carlo programs: the POWHEG BOX", *JHEP* **06** (2010) 043, `doi:10.1007/JHEP06(2010)043`, `arXiv:1002.2581`.

[38] J. Allison et al., "Geant4 developments and applications", *IEEE Trans. Nucl. Sci.* **53** (2006) 270, `doi:10.1109/TNS.2006.869826`.

[39] CMS Collaboration, "Performance of muon identification in pp collisions at s**0.5 = 7 TeV", Technical Report CMS-PAS-MUO-10-002, CERN, 2010. Geneva, 2010.

[40] CMS Collaboration, "Identification of b-quark jets with the CMS experiment", *JINST* **8** (2013) P04013, `doi:10.1088/1748-0221/8/04/P04013`, `arXiv:1211.4462`.

[41] CMS Collaboration, "Measurement of $t\bar{t}$ production with additional jet activity, including b quark jets, in the dilepton decay channel using pp collisions at $\sqrt{s} = 8\,\text{TeV}$", *Eur. Phys. J.* **C76** (2016), no. 7, 379, `doi:10.1140/epjc/s10052-016-4105-x`, `arXiv:1510.03072`.

[42] CMS Collaboration, "Measurement of the cross section ratio $\sigma_{t\bar{t}b\bar{b}}/\sigma_{t\bar{t}jj}$ in pp collisions at $\sqrt{s} = 8\,\text{TeV}$", *Phys. Lett.* **B746** (2015) 132–153, `doi:10.1016/j.physletb.2015.04.060`, `arXiv:1411.5621`.

[43] CMS Collaboration, "Measurement of the top quark mass using proton-proton data at $\sqrt{(s)} = 7$ and 8 TeV", *Phys. Rev.* **D93** (2016), no. 7, 072004, `doi:10.1103/PhysRevD.93.072004`, `arXiv:1509.04044`.

[44] M. Czakon and A. Mitov, "Top++: A Program for the Calculation of the Top-Pair Cross-Section at Hadron Colliders", *Comput. Phys. Commun.* **185** (2014) 2930, `doi:10.1016/j.cpc.2014.06.021`, `arXiv:1112.5675`.

[45] CMS Collaboration, "Measurement of the differential cross section for top quark pair production in pp collisions at $\sqrt{s} = 8\,\text{TeV}$", *Eur. Phys. J.* **C75** (2015), no. 11, 542, `doi:10.1140/epjc/s10052-015-3709-x`, `arXiv:1505.04480`.

[46] M. Czakon, D. Heymes, and A. Mitov, "High-precision differential predictions for top-quark pairs at the LHC", *Phys. Rev. Lett.* **116** (2016), no. 8, 082003, `doi:10.1103/PhysRevLett.116.082003`, `arXiv:1511.00549`.

[47] N. Kidonakis, "NNLL threshold resummation for top-pair and single-top production", *Phys. Part. Nucl.* **45** (2014), no. 4, 714–722, `doi:10.1134/S1063779614040091`, `arXiv:1210.7813`.

[48] CMS Collaboration, "Determination of jet energy calibration and transverse momentum resolution in CMS", *Journal of Instrumentation* **6** (November, 2011) 11002, `doi:10.1088/1748-0221/6/11/P11002`, `arXiv:1107.4277`.

[49] CMS Collaboration, "Performance of b tagging at sqrt(s)=8 TeV in multijet, ttbar and boosted topology events", Technical Report CMS-PAS-BTV-13-001, CERN, Geneva, 2013.

[50] CMS Collaboration, "CMS Luminosity Based on Pixel Cluster Counting - Summer 2013 Update", Technical Report CMS-PAS-LUM-13-001, CERN, Geneva, 2013.

[51] L. Moneta et al., "The RooStats Project", *PoS* **ACAT2010** (2010) 057, `arXiv:1009.1003`.